J Mater Sci (2019) 54:13775–13786

Metals & corrosion

Effect of austenitisation temperature on corrosion resistance properties of dual-phase high-carbon steel

Wilson Handoko[1,*], Farshid Pahlevani[1], and Veena Sahajwalla[1]

[1] *Centre for Sustainable Materials Research and Technology (SMaRT Centre), School of Materials Science and Engineering, UNSW Sydney, Sydney, NSW 2052, Australia*

Received: 16 January 2019
Accepted: 21 July 2019
Published online: 26 July 2019

ABSTRACT

Austenitisation is one of the most important factors in heat treatment process of dual-phase high-carbon steel, as it can affect the grain size, production of secondary phase precipitation, size of martensite laths and distribution of the phases. Despite the importance of this heat treatment on mechanical behaviour, its correlation on corrosion behaviour and electrochemical properties of high-carbon steel required in-depth investigation. The aim of this study is to investigate the effect of different austenitising temperatures on microstructure and corrosion behaviour of dual-phase high-carbon steel. Microstructural evolution was observed in situ using ultra-high-temperature laser microscope, and the steels have been characterised further using optical microscope, electron backscatter diffraction, 3D laser scanning confocal microscope, scanning electron microscope and energy energy-dispersive spectroscope and electron probe microanalysis. The powerful electrochemical corrosion test was employed by using Tafel polarisation method to measure its corrosion rate. Results have indicated that higher austenitising temperature increased grain size of retained austenite and martensite, which reduced the grain boundary length, but at the same time increased the size and amount of carbide precipitations. As the main corrosion mechanisms in dual-phase high-carbon steel were pitting corrosion and intergranular corrosion, effect of generated precipitations has overcome grain boundary corrosion caused by influence of size and shape of microstructures and, thus, reduced the corrosion resistance around 9.68% as temperature increased. These findings are crucial for designing new applications from high-carbon steels for mining and automotive industries.

Address correspondence to E-mail: w.handoko@unsw.edu.au

https://doi.org/10.1007/s10853-019-03859-0

Introduction

In recent years, the utilisation of high-carbon steel has inevitably increased in different area, such as mining, construction, gas and transport industries due to its superior hardness and abrasion resistance. But each of these applications brings different corrosive circumstances [1–3]. In mining area, one of the greatest constraints is the lack of groundwater for mining activities due to its remote location with limited access to water resource. The alternate used of seawater or desalinated water is more accessible and affordable in such environment across the industry operation [4]. Dual-phase high-carbon steel consisted of dual-phase microstructures, retained austenite and martensite. To achieve the optimum microstructure properties, identifying the best austenitising heat treatment temperature and time is required, as it is one of the most important steps to produce the desire mechanical properties without modifying the compositional elements. With high carbon content in this grade of steel, the existence of any carbides generated during production of this steel was essentially unavoidable, but the steel became homogenised through austenitising heat treatment stage, as undissolved carbides can be dissolved. However, at the same time by increasing the austenitising temperature, the potential formation of other secondary phases can increase [5]. Upon maintaining different austenitising temperatures, average grain size and phase distribution can change, which can result in different properties, especially in its corrosion resistance of high-carbon steel. But at the same effect of this heat treatment process on precipitation of secondary phases is indivertible and need to be studied in detail [6, 7].

By increasing austenitisation temperature, average grain size of parent austenitic phase increases, which results in larger retained austenite grains and larger martensite laths at room temperature upon quenching stage [8]. In addition to increasing the grain size, higher austenitising temperature can lead to increasing the risk of generating more secondary precipitation, impurity segregation on grain boundary and random boundary network that will cause higher rate of intergranular corrosion (IGC) on interboundary [9, 10]. IGC was due to deterioration along the grain boundary because thermodynamic effect for susceptibility towards corrosion is higher at grain boundary than at inner grain boundary caused by exposure of certain crystalline in steels, secondary phase precipitations and compositional difference at a circumstance (e.g. electrochemical) [9, 10]. Other types of corrosion could possibly occur—grain boundary corrosion due to difference in potential energy of constituent phases (e.g. dual-phase microstructure), where one phase became preferential attack than another as it contained different Fe and C balance in each phase [10, 17]. Additionally, pitting corrosion or localised corrosion was caused by passivation process at certain area on steel that initiated anodic and cathodic half reaction and, thus, led to electromigration of anions and potential gradient, which began the pit growth with limited amount of diffusion of ions [10, 11]. As grain size increased, the influence of its electrochemical corrosion behaviour on steel can increase, this was due to increase in atom movement (velocity) prior to the corrosion process reaction [11, 12]. Previous studies by Handoko et al. [13, 14] suggested that blocky and larger grain size of retained austenite with increased in its volume fraction phase and could decrease its grain boundary density, which led to lower corrosion intensity rate. Heat treatment or grain refinement processing has altered the reactivity of the microstructure on lower C and higher Mn content steels in which can impact on corrosion resistance and oxide formation response and the presence of precipitation increased weak points in structural [15, 16]. The main reason for enhancement in corrosion resistance properties in refining grain size was corresponded to increase in generated passive film and adhesion, since it led to increase density in the grain boundary [17, 18].

For identifying the best application for this grade of steel, correlation size, shape and arrangement of microstructural phases and corrosion characteristic should be discreetly determined. In this study, we carefully analysed the influence of grain size and precipitation of secondary phases on corrosion behaviour of dual-phase high-carbon steel in NaCl solution and its electrochemical properties. The microstructural transformation throughout different austenitisation temperatures was observed through in situ ultra-high-temperature laser microscopy, microstructural analysis by optical microscopy, electron backscatter diffraction microscopy (EBSD), 3D laser scanning confocal microscope (3D LSCM), scanning electron microscope (SEM) and electron probe microanalysis (EPMA). Identifying volume fraction of secondary phases precipitation by ImageJ

and corrosion potential, E_{corr} and current, i_{corr} to define corrosion rate through reliable electrochemical test of Tafel Polarisation technique.

Materials and methods

Material preparation

Dual-phase high-carbon steel with nominal chemical composition 1.00C, 0.98Mn, 0.60Cr and 0.20Si (in wt%) was used in this study. Metallographic sample preparation was conducted; the steel was precisely cut into three pieces with 10 × 10 × 3 mm dimension by Accutom-50 with slow feeding speed mode at 6 mm/min to prevent shear stress and heat transfer that can lead to spontaneous phase transformation. Then all samples were grinded with SiC paper to 4000 grits by TegraPol-21 and polished with fine diamond suspension to 0.1 μm by TegraPol-15 in the way that fitted into the 10-mm-diameter alumina crucible size for heat treatment experiment. The mirror-polished samples were heated by ultra-high-temperature laser microscope CLM VL2000DX that provides in situ observation of microstructural changes. At the beginning, chamber was vacuumed to remove any unattended gases that can initiate oxidation during the experiment. Additionally, helium gas was kept into standby mode for cooling/quenching purpose. All samples were heated to different temperatures at 950 °C, 1050 °C and 1150 °C with heating rate at 500 °C/min, dwelling time for 10 min, cooling rate at − 3000 °C/min to obtain similar volume fraction of retained austenite and martensite phases, and pressure in the chamber was kept about 6.5 kPa during the experiment. 3.5% NaCl solution was prepared and immersed into the media for corrosion test at 1 h and 2 h at 24 °C ± 1. All samples were ultrasonic cleaned by Unisonics to eliminate corrosion product and completely dried by Struers Drybox-2.

Analytical methods

Volume fraction of precipitated secondary phases at the austenitisation temperature was determined by image analyser, ImageJ. Microstructural analysis was conducted using optical microscopy, Nikon Eclipse ME600. High reconstruction electron backscatter diffraction microscopy (EBSD) was achieved by employing JEOL 7001F that equipped with Schottky field emission gun scanning electron microscopy (FE-SEM) and Everhart–Thornley secondary electron detector for topographical imaging. Acquired images were processed with orientation imaging microscopy (OIM) version 8 software to obtain valuable information volume fraction of each phase and its distribution grain boundary mappings. Two sets of corrosion tests were demonstrated in this study: immersion method and electrochemical measurement. 3D laser scanning confocal microscope—VK-X250 3D LSCM—was implemented for non-destructive high-resolution three-dimensional surface roughness imaging before and after corrosion; surface area of mean roughness average (S_a), surface area of ten-point means roughness (S_z) and surface area of measured pit growth (S_{pg}) values can be determined by VK Viewer software—immersion method. Other surface imaging was predominantly used by SEM Hitachi S-3400I with accelerating voltage of 20 keV and emission current 60 μA—immersion method. This SEM instrument was equipped with EDS analysis to determine the chemical composition of corrosion product. Elemental analysis was up to sub-micron level on steel substrate samples by electron probe microanalysis (EPMA)—JEOL JXA-8500F. Electrochemical measurements were taken by Versatile Multipotentiostat VSP300 that equipped with EC-Lab v11.02 software. This instrument was connected to a corrosion flat cell with saturated calomel electrode (SCE) as reference electrode, platinum electrode as auxiliary electrode and high-carbon steel sample as working electrode. The 3.5 wt% NaCl solution was utilised as electrolyte for the corrosion test experiments, and contacted area of tested steel sample was 1 cm^2 in open-circuit potential (OCP) system with 4 h of immersion time. Results of Tafel curves were collected and compiled between (± 250 mV vs. OCP) and (± 250 mV vs. OCP), scan rate at 0.003 V/min and bandwidth of 8. The values of corrosion potential, E_{corr} and corrosion current i_{corr} can be determined through polarisation curves to evaluate corrosion rate of each steel sample.

Data availability

The data that support the findings of this study are available from the corresponding author upon reasonable request.

Results and discussions

Before corrosion conducting corrosion test, it is important to understand the effect of austenitising temperature on generated austenite grain size, shape and structure. In situ observation from ultra-high-temperature confocal laser microscope was compiled and compared the dissimilarity in austenite phase size and shape and secondary phase distribution at the last seconds before quenching process. Figure 1 summarises these results which include a diagonal yellow line overlayed from top left to bottom right side as the standard procedure to calculate austenitic grain size. Nine-sided images were recorded and average grain size values of each different austenitising temperature were calculated.

Calculation of grain size, G, for all different heating temperature was based on the standard ASTM grain size formula, where L refers to average intercept grain size in mm unit [19], as follows:

$$G = -3.2877 - 6.6439 \log_{10}\left(\frac{L}{1000}\right)$$

As it was expected by increasing the austenitising temperature, average intercept grain size increased, Table 1. This increase in austenite grain size had fulfilled the agreement as per study from Li et al. [20] and Ovali et al. [21] on the thermal stability of retained austenite in austenitising temperature.

By increasing the austenitising temperature and grain growth associate with that, the length of grain boundary reduces but at the same time the number of precipitated secondary phase increased [22, 23]. Figure 2 presents the comparison of microstructural analysis of dual-phase steel samples at different heat-treated temperatures. It can be seen that there is obvious difference in grain size, shape and arrangement of each phase. The quantity and size of carbide formation were increased as austenitising temperature elevated and thus enhanced the risk on intergranular attack (IGA) and cracking [24]. Also, as the temperature increased, grain growth, size and shape for both retained austenite and martensite had gradually expanded [25].

Table 1 Comparison of the effect of different austenitising temperature on the ASTM grain size number and average intercept grain size was determined though nine-sided in situ observation by confocal microscopy

Sample-ID (°C)	ASTM grain size number	Average intercept grain size (μm)
950	4.6	65.3
1050	4.0	80.3
1150	3.1	107.5

To understand the influence of different austenitising temperatures on this grade of steel, a non-destructive analysis on each phase was imperative before corrosion test by utilising EBSD micrograph in Fig. 3. It is clearly visible to observe the variation in size, shape and arrangement each phase from micrograph images. From the quantitative data of OIM software, the EBSD micrograph presented approximately 14.1%, 13.3% and 17.7% percentage of retained austenite, at austenitising temperature of 950 °C, 1050 °C and 1150 °C, respectively. The volume fraction of retained austenite and martensite phase was relatively similar. Moreover, previous research had been performed on the effect of finer grain size, which could lead to higher risk of

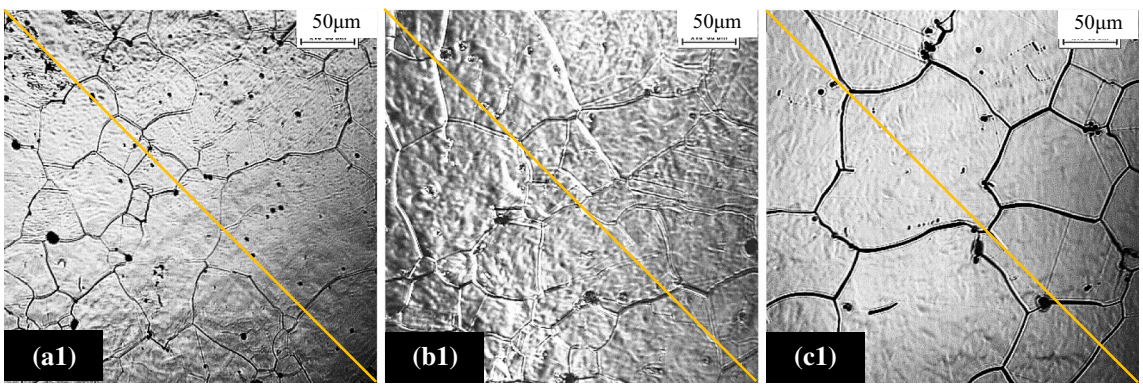

Figure 1 Images comparison from ultra-high-temperature laser microscopy of different austenite grain sizes during austenitising temperature at **a1** 950 °C, **b1** 1050 °C and **c1** 1150 °C.

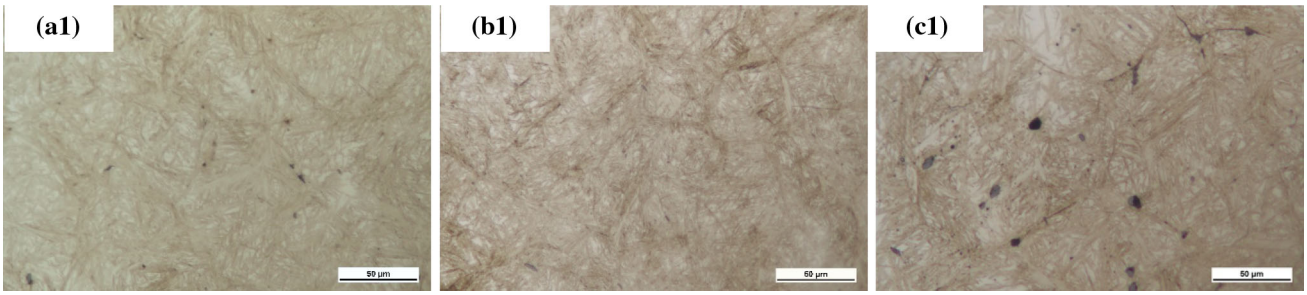

Figure 2 Optical microscope imaging of dual-phase high-carbon steel after heat treatment at **a1** 950 °C, **b1** 1050 °C and **c1** 1150 °C, with light etching condition—volume fraction of each phase can be calculated through EBSD analysis.

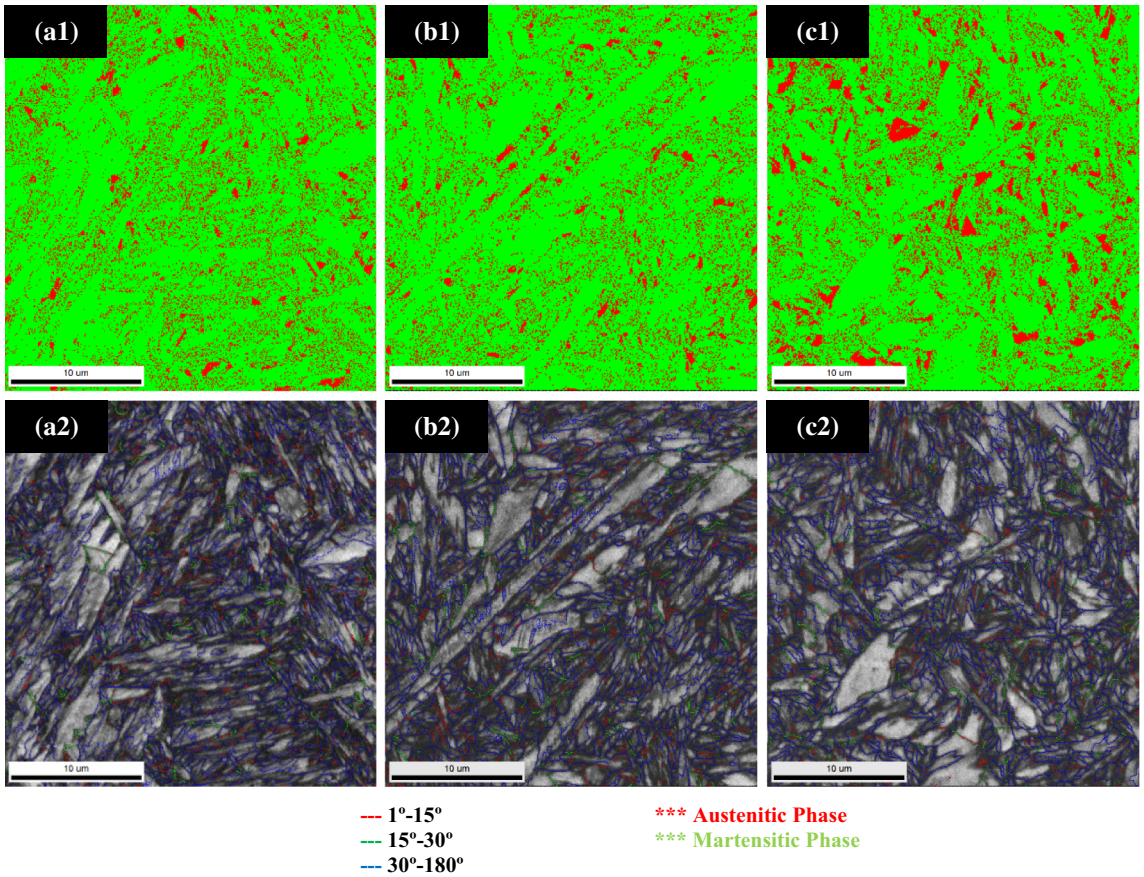

Figure 3 EBSD micrographs of retained austenite and martensite phases distribution mapping at **a1** 950 °C, **b1** 1050 °C and **c1** 1150 °C, red phase is retained austenite and green is martensite phase, with grain boundary mapping **a2** 950 °C, **b2** 1050 °C and **c2** 1150 °C, red line is grain boundaries at 1°–15°, green line is grain boundaries at 15°–30°, and blue line is grain boundaries at 30°–180°.

susceptibility towards grain boundary corrosion, thus reducing corrosion resistance properties [26]; this means by decreasing contact between inter-boundary of retained austenite and martensite phases, corrosion rate can be reduced [11]. Further morphological imaging and electrochemical measurement were required to understand the effect of different austenitising temperatures on corrosion resistance performance of dual-phase high-carbon steel.

To understand the corrosion mechanism of this grade of steel, a schematic diagram of corrosion process was explained. Thermodynamics of corrosion reaction, mechanism and pit growth in the corrosion

process on high-carbon steel at given immersion time with the chemical composition of corrosion product is presented in Fig. 4. At the beginning stage or 0 h, the pit growth initiated from structural or localised chemical defects on surface of steel; then after 1 h the pit began to expand and production of corrosion product, $Fe(OH)_3$, occurred due to Fe^{2+} dissolution process on the steel surface, leaving a negative charge (e^-) in steel. Finally, there is continuous development of pit growth and increased amount of corrosion product. At the pit areas, anodic reaction caused the Fe to dissolve (dissolution of iron) from onset of immersion through chemical reaction of:

$$Fe \rightarrow Fe^{2+} + 2e^-$$

At the same time, the O_2 reduction–cathodic reaction developed near the steel surface, as electrons have given up by anode flow to cathode where discharging occurred.

$$O_2 + 2e^- + 2H_2O \rightarrow 4OH^-$$

As consequences of these reactions, electrolyte has enclosed in the pit area received positive charge in comparison with electrolyte around the pit that has become negatively charged. This positively charged interested in negative ions, Cl^-, which the

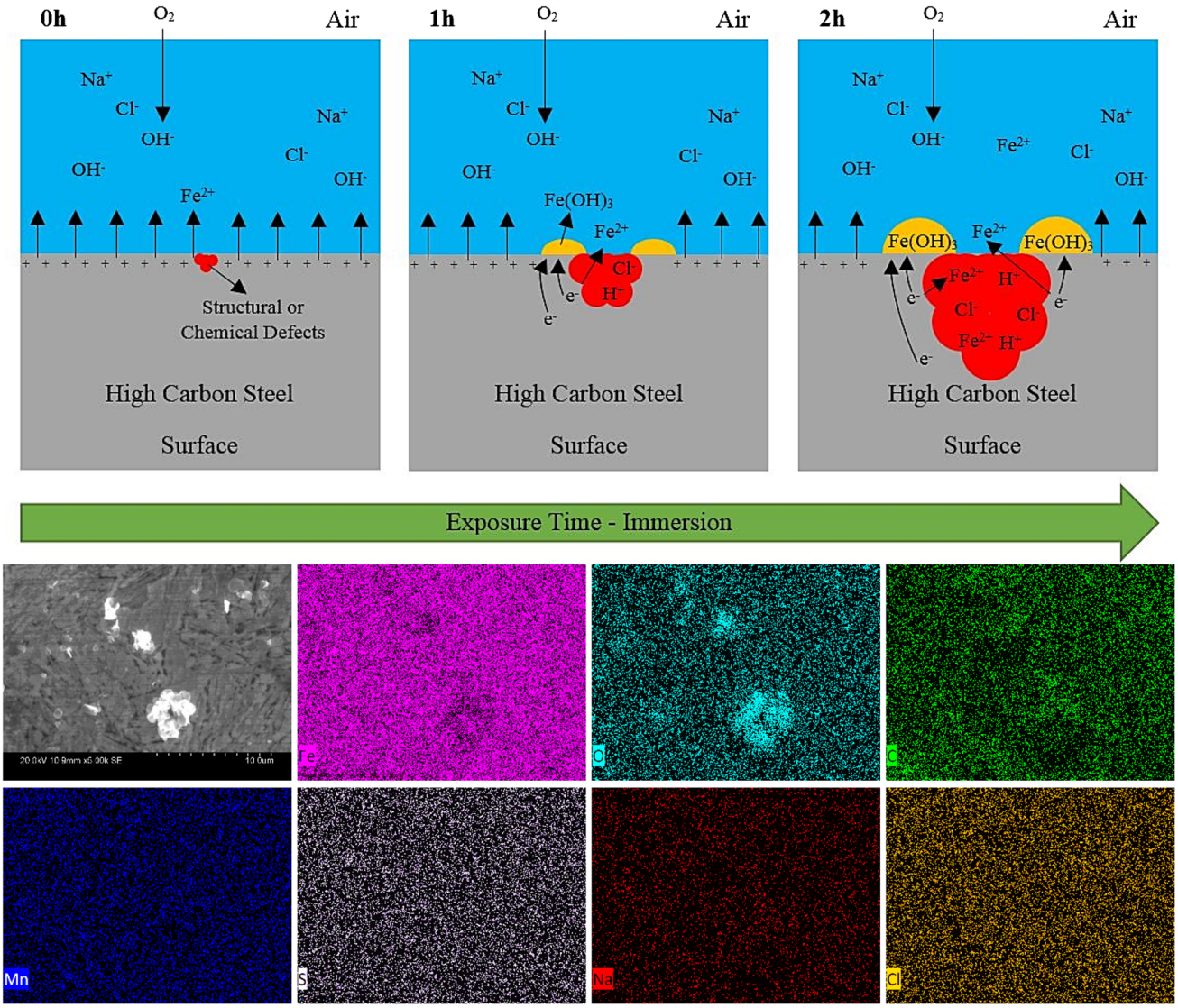

Figure 4 The schematic of corrosion mechanisms—pit growth on dual-phase high-carbon steel immersed into 3.5 wt% NaCl solution. Chemical composition of corrosion product was analysed by SEM/EDS.

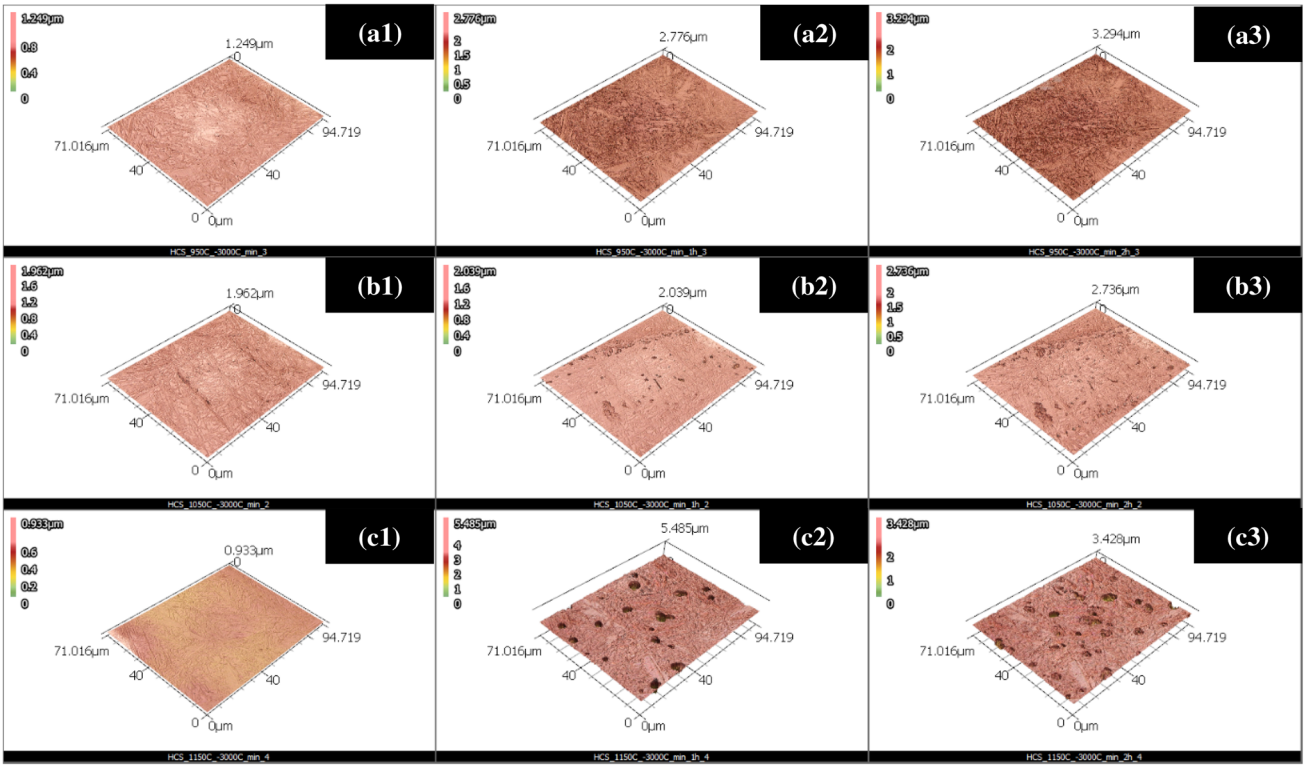

Figure 5 3D imaging by laser scanning confocal microscopy in 3.5 wt% NaCl solution for **a1** 0 h, **a2** 1 h, **a3** 2 h for samples at 950 °C; **b1** 0 h, **b2** 1 h, **b3** 2 h for samples at 1050 °C; and **c1** 0 h, **c2** 1 h, **c3** 2 h for samples at 1150 °C. Values of S_a, S_z and S_{pg} of each sample were determined.

thermodynamically favour reaction can be found in reaction, as follows:

$$FeCl_2 + 2H_2O \rightarrow Fe(OH)_2 + 2HCl$$

Therefore, as steel surface exposed continued, the corrosion product, $Fe(OH)_3$, formed as per agreement with EDS results.

The corrosion test was performed for all steel samples at 1 h and 2 h though immersion test into 3.5 wt% NaCl solution. Three-dimensional high-resolution topographical imaging was generated by 3D LSCM before and after corrosion, as illustrated in Fig. 5.

Retained austenite and martensite phases for all samples have been revealed at 0 h or after light etching condition. For sample-950 °C at 1 h after corrosion, the morphology was slightly degraded as preferential attack on retained austenite and martensite remained unmodified. Main aspect of this preferential attack was due to higher Fe content and lower C content on retained austenite than martensite; hence, austenite acted as anode, whereas martensite acted as cathode [13, 14]. Multiple tiny pores from carbide precipitation were generated at 2 h of corrosion on austenite and slight deterioration on martensitic phase. While sample-1050 °C performed moderate damage on austenite with pit growth due to breakdown of passive film and followed by slight changed on martensite after 1-h corrosion process, this phenomenon continued and larger pit holes were generated. As more secondary phases precipitated, meaning that increased the potential to initiate IGC between both interfaces than in 950 °C. Moreover, sample which heat-treated at 1150 °C showed severe damage on retained austenite with numerous pitting holes appeared with moderate damage on martensite phase after first hour of corrosion; more degradation on both phases occurred with massive pit growth. This factor was caused by precipitation of more precipitated secondary phases which distinctively reduced the percentage of C and Mn content in austenite and martensite phases [27]. From 3D LSCM, it can be observed that influence of different austenitising temperatures had side effect on the corrosion behaviour, as more precipitation generated and depletion of retained austenite and

Table 2 Surface area values of S_a, S_z and S_{pg} before and after corrosion in 3.5 wt% NaCl solution

Time (h)	950 °C			1050 °C			1150 °C		
	S_a (μm)	S_z (μm)	S_{pg} (μm)	S_a (μm)	S_z (μm)	S_{pg} (μm)	S_a (μm)	S_z (μm)	S_{pg} (μm)
0	0.018	1.013	–	0.021	1.205	–	0.022	1.228	–
1	0.029	2.124	0.011	0.034	2.437	0.013	0.096	3.665	0.074
2	0.039	2.993	0.021	0.046	3.199	0.025	0.151	4.995	0.129

martensite from C and Mn can lead to higher propensity on pitting corrosion.

From VK Viewer software, quantitative data of surface area of mean roughness average (S_a), ten-point mean roughness (S_z) and measured pit growth (S_{pg}) values were compiled, as shown in Table 2. It can be outlined that S_a value was the highest at sample-1150 °C, accounted 0.151 μm nearly five times higher compared to sample-950 °C with 0.039 μm after 2 h of corrosion test. Meanwhile, the value of S_z was the highest on the sample with highest austenitised temperature amongst all samples. Overall, as the grain size of retained austenite and martensite was increased at higher heating temperature, the S_a and S_z values increased with escalated value of S_{pg} since more precipitation occurred that led to increase in boundary corrosion and larger size of pit growth, thus promoted higher level of corrosion intensity.

SEM imaging analysis was adopted for further microstructural investigation before and after corrosion test. With secondary electron (SE) mode, it provided a clear morphology of both austenitic and martensitic interfaces reacted towards corrosion behaviour in 3.5 wt% NaCl media, as presented in Fig. 6. It can be analysed that by increased austenitising temperature, the corrosion intensity and microstructural degradation had been inclined. These sections had been imprinted with circle in Fig. 6 that helped in trailing the modification of the surface morphology during 2-h corrosion process. For sample-950 °C, it remained almost unchanged after 1 h and slight changed in austenite phase with numbers of tiny pit holes generated surround grain boundary after 2 h. On the other hand, sample-1050 °C performed deterioration on austenite with initiation of pit holes after 1 h and more damage on this phase followed by martensite phase occurred after 2 h. At higher heating temperature, it increased the risk of carbide precipitation that could trigger early IGA in the vicinity of boundary. In comparison with sample-1150 °C, serious damage occurred on retained austenite phase with multiple larger size pit holes happened after 1 h, and more destruction on austenitic phase as well as moderate-scale degradation on martensitic phase. There is a formation of larger grain size on both phases and more secondary phase precipitation on grain boundary, because higher austenitising temperature will be more prevalent in determining the corrosion-resistant property of dual-phase steel, thus with blocky, lengthy and unordered boundary packet which can correlate to higher corrosion rate. From this SEM analysis, it can be summarised that higher austenitising temperature of dual-phase high-carbon steel sample had a great contribution on increasing grain size of retained austenite–martensite and produced more carbide, as well as enhancing IGC and grain boundary corrosion that can reduce its corrosion resistance properties.

To quantify and reliably investigate the formation of different secondary phases during austenitisation process, a powerful microanalytical method was implemented to detect various elements that formed different type of secondary phase precipitation on steel. EPMA analysis data which presented in Fig. 7 indicated the formation of three different precipitations, such as manganese sulphide (MnS), iron carbide (Fe_3C) and silicon oxide (SiO_2). These precipitations promoted localised electrochemical attack on grain boundaries of steel, which is visible in microstructural analysis after different corrosion times in Fig. 6. Different size of pitting corrosion growth was attributed to the size and distribution of these precipitated secondary phases which modified its corrosion resistance properties [28, 29]. As a result, combination of non-uniform boundary distribution and increased risk of pitting corrosion and IGC initiation on samples with higher austenitisation temperature can lead to higher-level susceptibility on corrosion degradation.

One of the most reliable techniques for electrochemical corrosion measurement was implemented

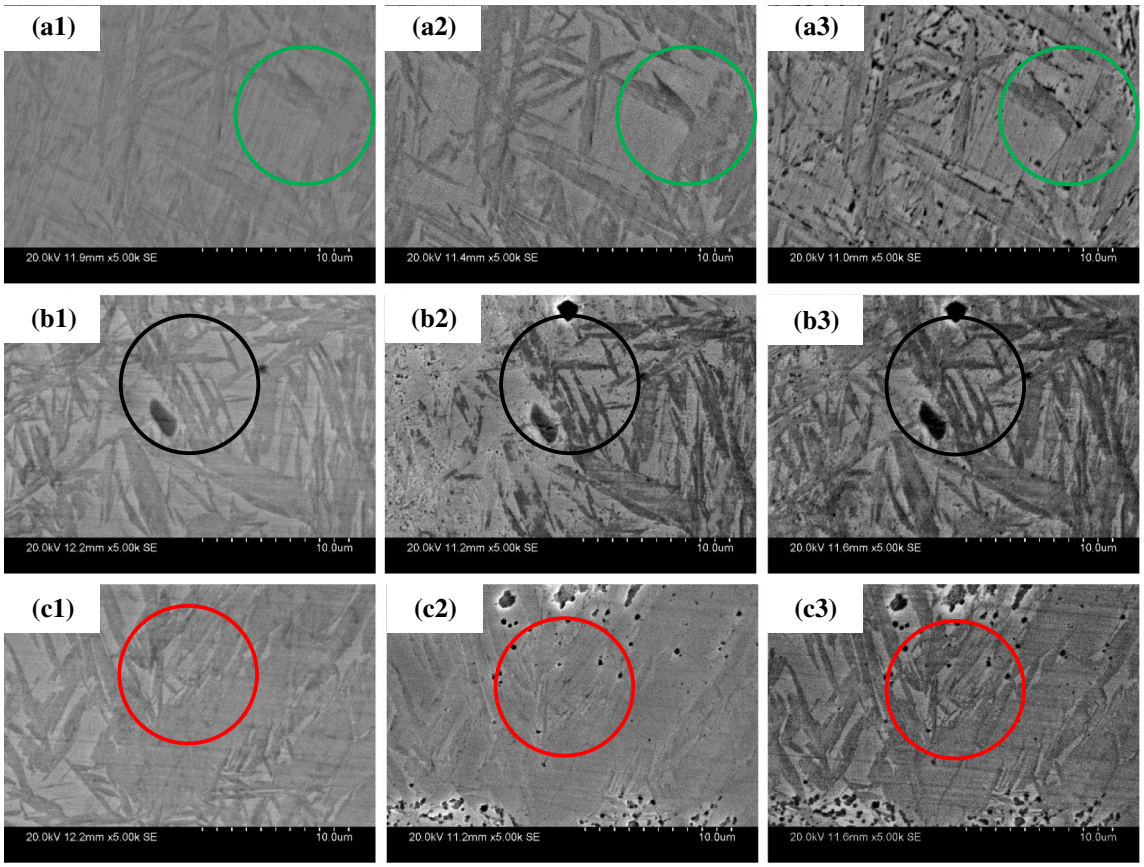

Figure 6 Morphological images from SEM analysis of three different steel samples before (yet after etched) and after immersion into 3.5 wt% NaCl solution, temperature at **a1** 0 h, **a2** 1 h, **a3** 2 h for samples at 950 °C; **b1** 0 h, **b2** 1 h, **b3** 2 h for samples at 1050 °C; and **c1** 0 h, **c2** 1 h, **c3** 2 h for samples at 1150 °C.

to determine Tafel polarisation curves which were valuable to predict corrosion rate. From Tafel polarisation curve, total corrosion current density can be found between intersect of anodic (top side) and cathodic (bottom side) branches. The anodic branch represented the passivation, the formation of corrosion products and degradation of the steel samples, whereas cathodic branch demonstrated the activation control and hydrogen formation. In Fig. 8, Tafel polarisation curves were produced, presented by increased austenitising temperature which could lead to increase in corrosion rate value on dual-phase high-carbon steels. The formation of different types of secondary phase precipitation at higher austenitising temperature had played a crucial effect on IGC around contacted boundaries and hence can increase the risk of pit growth [30, 31]. More precipitations occurred along the grain boundary of both retained austenite and martensite interfaces, the higher potential of grain boundary reaction on, along and within grain boundary.

The quantitative data had been recorded and are summarised in Table 3. This table showed different material properties as the effect of various austenitising temperatures that led to variable in corrosion potential values, E_{corr}, where shifted to more positive direction had higher-level of corrosion resistance properties. It can be stated that sample-950 °C had the lowest tendency on corrosion reaction initiation than other higher austenitisation temperature samples. Value i_{corr} gap on sample-950 °C was 5.22% and 9.68% lower than sample-1050 °C and sample-1150 °C, respectively. For E_{corr} value of sample-950 °C accounted about 4.50% lower than sample-1050 °C and 9.16% on sample-1150 °C accordingly towards more noble side. Evidence of the highest i_{corr} occurred on the highest heated sample in which the presence of highest precipitated carbide proved its significant effect on corrosion rate; hence, higher heating temperature had influence on reduction in corrosion resistance properties.

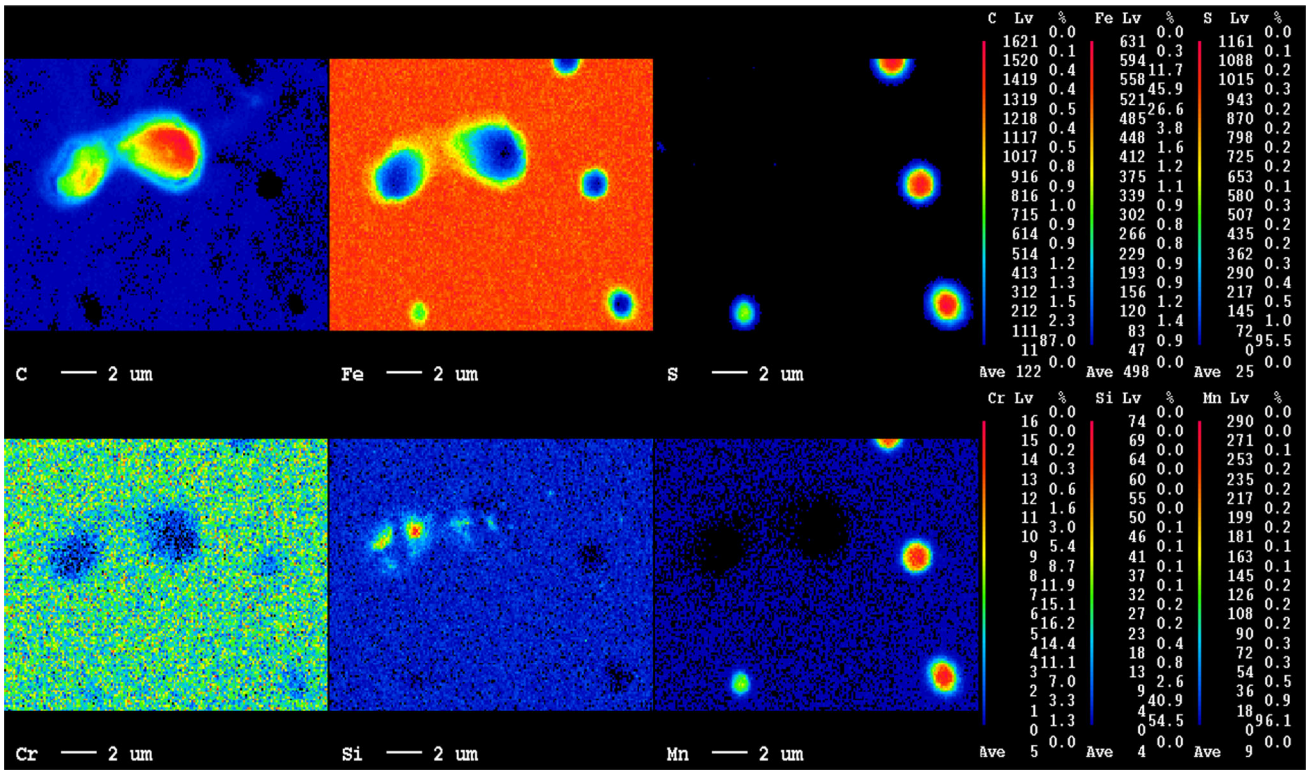

Figure 7 EPMA analysis of C, Fe, S, Cr, Si and Mn for the heat-treated sample at 1150 °C.

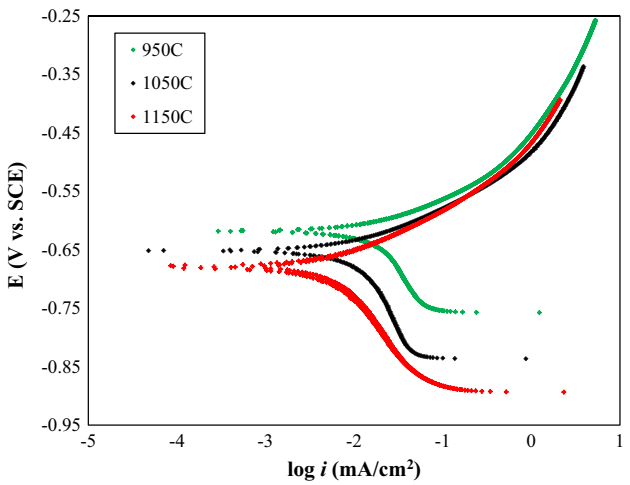

Figure 8 The comparison of Tafel polarisation curves from different austenitising temperatures of high-carbon steels into 3.5 wt% NaCl solution condition.

This approach in the study had clearly emphasised that corrosion intensity obtained by electrochemical measurement technique could be added by different in-depth morphological analysis for conscientious characterisation of corrosion resistance properties on high-carbon steel. Furthermore, corrosion mechanisms that appeared in this study were pitting corrosion and IGC, initiating from grain boundary between retained austenitic and martensitic planes with preferential attack on austenitic phase as more and larger size of precipitation was produced. This study has demonstrated that when the main corrosion mechanism is the pitting corrosion, effect of the volume and size of secondary phase plays more important role in corrosion behaviour compared to the length of grain boundaries.

Table 3 The summarised electrochemical data for dual-phase high-carbon steels in 3.5 wt% NaCl solution

Sample-ID (°C)	E_{corr} (mV vs. SCE)	i_{corr} (mA/cm^2)
950	− 622 ± 5	1.993 ± 0.003
1050	− 650 ± 4	2.097 ± 0.007
1150	− 679 ± 6	2.186 ± 0.005

Conclusions

Corrosion resistance of dual-phase high-carbon steels at different austenitisation temperatures has been studied and investigated in-depth . Results have

revealed that by increasing the austenitising temperature, the pre-austenite grain size increased, which promoted larger retained austenite grain with bulky martensite laths. Increase in temperature corresponded to the increase amount of secondary phase precipitation. Preferential attack on one phase in this dual-phase steel–retained austenite followed by martensite, is due to higher Fe content in retained austenite phase, which acted as anode. With larger grain size, it decreased the propensity towards corrosion degradation, due to decrease in grain boundary density, and reduced the potential energy gap between each phase and improved the stability of retained austenite. The volume of secondary phase precipitation has been increased through higher austenitisation temperature, which has attributed to increase the risk of generating pit growth, thus accelerated the overall corrosion rate. Electrochemical corrosion measurements have validated that the lowest current density and most positive corrosion potential values towards noble side from Tafel polarisation curves emerged on the lowest heat-treated steel at 950 °C, leading to the best corrosion resistance than all studied steels, improved approximately 9.68%. This investigation has performed that primary corrosion mechanisms were pitting, with the presence of precipitations promoted IGA that become the major roles in corrosion behaviour on dual-phase high-carbon steel, has overcome the influence of grain boundary corrosion that caused by different size, shape and distribution of constituent phases.

Acknowledgements

This research was supported under Australian Government Research Training Program (RTP) and Australian Research Council's Industrial Transformation Research Hub funding scheme (Project IH130200025). We gratefully acknowledge the technical support provided by the Analytical Centre in UNSW Sydney.

Author's contribution

Wilson Handoko performed experiments and data analysis. Farshid Pahlevani designed the project and experiments and critically analysed the data. Veena Sahajwalla supervised the study and gave recommendations to revise manuscript. Wilson Handoko wrote the manuscript and all authors analysed data, discussed the results, read and approved the final manuscript.

Compliance with ethical standards

Conflict of interest The authors declare that they have no conflict of interest.

References

[1] Yonezu A, Kusano R, Chen X (2012) On the mechanism of intergranular stress corrosion cracking of sensitized stainless steel in tetrathionate solution. J Mater Sci 48(6):2447–2453. https://doi.org/10.1007/s10853-012-7032-8

[2] Xiong L, You Z, Lu L (2016) Enhancing fracture toughness of nanotwinned austenitic steel by thermal annealing. Scripta Mater 119:55–59

[3] Zheng Z, Zheng Y (2016) Erosion-enhanced corrosion of stainless steel and carbon steel measured electrochemically under liquid and slurry impingement. Corros Sci 102:259–268

[4] Kamrunnahar M, Urquidi-Macdonald M (2010) Prediction of corrosion behavior using neural network as a data mining tool. Corros Sci 52(3):669–677

[5] Chen C, Chen C, Yang J (2015) Synergistic effect of austenitizing temperature and hot plastic deformation strain on the precipitation behavior in novel HSLA steel. Mater Sci Eng, A 639:145–154

[6] Lee J, Kang N, Park J, Ahn S, Park Y, Choi I, Kim K, Cho K (2011) Kinetics of carbide formation for quenching and tempering steels during high-frequency induction heat treatment. Mater Chem Phys 129(1–2):365–370

[7] Liu Z, Gao X, Li J, Du L, Yu C, Li P, Bai X (2016) Corrosion behaviour of low-alloy martensite steel exposed to vapour-saturated CO_2 and CO_2—saturated brine conditions. Electrochim Acta 213:842–855

[8] Wang D, Kahn H, Ernst F, Heuer A (2015) NiAl precipitation in delta ferrite grains of 17-7 precipitation-hardening stainless steel during low-temperature interstitial hardening. Scripta Mater 108:136–140

[9] Shimada M, Kokawa H, Wang Z, Sato Y, Karibe I (2002) Optimization of grain boundary character distribution for intergranular corrosion resistant 304 stainless steel by twin-induced grain boundary engineering. Acta Mater 50(9):2331–2341

[10] Isfahany A, Saghafian H, Borhani G (2011) The effect of heat treatment on mechanical properties and corrosion

behavior of AISI420 martensitic stainless steel. J Alloy Compd 509(9):3931–3936

[11] Li Y, Wang F, Liu G (2004) Grain size effect on the electrochemical corrosion behavior of surface nanocrystallized low-carbon steel. Corrosion 60(10):891

[12] Handoko W, Pahlevani F, Emmanuelawati I, Sahajwalla V (2016) Transforming automotive waste into TiN and TiC ceramics. Mater Lett 176:17–20

[13] Handoko W, Pahlevani F, Sahajwalla V (2017) Corrosion behaviour of dual-phase high carbon steel—microstructure influence. J Manuf Mater Process 1(2):21

[14] Handoko W, Pahlevani F, Sahajwalla V (2018) The effect of low-quantity Cr addition on the corrosion behaviour of dual-phase high carbon steel. Metals 8(4):199

[15] Devasenapathi A, Prasad R, Raja V (1996) Passivation and stress corrosion cracking tendency of manganese stainless steels. J Mater Sci 31(15):3989–3993. https://doi.org/10.1007/BF00352660

[16] Kainuma S, Jeong Y, Ahn J (2014) Investigation on the stress concentration effect at the corroded surface achieved by atmospheric exposure test. Mater Sci Eng, A 602:89–97

[17] Handoko W, Pahlevani F, Sahajwalla V (2018) Enhancing corrosion resistance and hardness properties of carbon steel through modification of microstructure. Materials 11(12):2404

[18] Jiang J, Liu Y, Chu H, Wang D, Ma H, Sun W (2017) Pitting corrosion behaviour of new corrosion-resistant reinforcement bars in chloride-containing concrete pore solution. Materials 10(8):903

[19] Peirson B (2005) Comparison of the ASTM comparative chart method and the mean line intercept method in determining the effect of solidification rate on the yield strength of AA5182. Laboratory Module 9 EGR 250—Materials Science and Engineering Section 1, 2005

[20] Li J, Zhang C, Jiang B, Zhou L, Liu Y (2016) Effect of large-size M 23 C 6 -type carbides on the low-temperature toughness of martensitic heat-resistant steels. J Alloy Compd 685:248–257

[21] Ovali I, Kilicli V, Erdogan M (2013) Effect of microstructure on fatigue strength of intercritically austenitized and austempered ductile irons with dual matrix structures. ISIJ Int 53(2):375–381

[22] Suski C, Oliveira C (2013) Effect of austenitization temperature on the precipitation of carbides in quenched low carbon boron steel. Metallogr Microstruct Anal 2(2):79–87

[23] Chen M, Yen H, Yang J (2013) The transition from interphase-precipitated carbides to fibrous carbides in a vanadium-containing medium-carbon steel. Scripta Mater 68(11):829–832

[24] Silva F, Santos J, Gouveia R (2017) Dissolution of grain boundary carbides by the effect of solution annealing heat treatment and aging treatment on heat-resistant cast steel HK30. Metals 7(7):251

[25] Chao Q, Cruz V, Thomas S, Birbilis N, Collins P, Taylor A, Hodgson P, Fabijanic D (2017) On the enhanced corrosion resistance of a selective laser melted austenitic stainless steel. Scripta Mater 141:94–98

[26] Ralston K, Birbilis N, Davies C (2010) Revealing the relationship between grain size and corrosion rate of metals. Scripta Mater 63(12):1201–1204

[27] Kokawa H, Shimada M, Sato Y (2000) Grain-boundary structure and precipitation in sensitized austenitic stainless steel. JOM 52(7):34–37

[28] Cervo R, Ferro P, Tiziani A, Zucchi F (2010) Annealing temperature effects on superduplex stainless steel UNS S32750 welded joints. II: pitting corrosion resistance evaluation. J Mater Sci 45(16):4378–4389. https://doi.org/10.1007/s10853-010-4311-0

[29] Tobie T, Hippenstiel F, Mohrbacher H (2017) Optimizing gear performance by alloy modification of carburizing steels. Metals 7(10):415

[30] Pardo A, Merino M, Coy A, Viejo F, Carboneras M, Arrabal R (2007) Influence of Ti, C and N concentration on the intergranular corrosion behaviour of AISI 316Ti and 321 stainless steels. Acta Mater 55(7):2239–2251

[31] Dryzek E, Sarnek M, Wróbel M (2014) Reverse transformation of deformation-induced martensite in austenitic stainless steel studied by positron annihilation. J Mater Sci 49(24):8449–8458. https://doi.org/10.1007/s10853-014-8555-y